④

AD-A197 956

# Picosecond Photoconductive Sampling Measurements of the Scattering Parameters of High-Speed Field-Effect Transistors

S. C. MOSS and D. D. SMITH
Chemistry and Physics Laboratory
Laboratory Operations
The Aerospace Corporation
El Segundo, CA 90245

22 August 1988
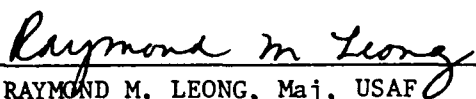
DTIC
ELECTE
AUG 2 9 1988
E

This report was submitted by The Aerospace Corporation, El Segundo, CA 90245, under Contract No. F04701-85-C-0086-P00019 with the Space Division, P.O. Box 92960, Worldway Postal Center, Los Angeles, CA 90009-2960. It was reviewed and approved for The Aerospace Corporation by S. Feuerstein, Director, Chemistry and Physics Laboratory.

Lt John K. Abreu/AFSTC/WCO was the project officer for the Mission-Oriented Investigation and Experimentation (MOIE) Program.

This report has been reviewed by the Public Affairs Office (PAS) and is releasable to the National Technical Information Service (NTIS). At NTIS, it will be available to the general public, including foreign nationals.

This technical report has been reviewed and is approved for publication. Publication of this report does not constitute Air Force approval of the report's findings or conclusions. It is published only for the exchange and stimulation of ideas.

JOHN K. ABREU, Lt, USAF
MOIE Project Officer
AFSTC/WCO OL-AB

RAYMOND M. LEONG, Maj, USAF
Deputy Director, AFSTC West Coast Office
AFSTC/WCO OL-AB

# REPORT DOCUMENTATION PAGE

| 1a REPORT SECURITY CLASSIFICATION | 1b RESTRICTIVE MARKINGS |
|---|---|
| Unclassified | |

| 2a SECURITY CLASSIFICATION AUTHORITY | 3 DISTRIBUTION/AVAILABILITY OF REPORT |
|---|---|
| | Approved for public release; |
| 2b DECLASSIFICATION/DOWNGRADING SCHEDULE | distribution unlimited. |

| 4 PERFORMING ORGANIZATION REPORT NUMBER(S) | 5. MONITORING ORGANIZATION REPORT NUMBER(S) |
|---|---|
| TR-0086A(2945-06)-2 | SD-TR-88-82 |

| 6a. NAME OF PERFORMING ORGANIZATION | 6b OFFICE SYMBOL (If applicable) | 7a. NAME OF MONITORING ORGANIZATION |
|---|---|---|
| The Aerospace Corporation Laboratory Operations | | Space Division |

| 6c. ADDRESS (City, State, and ZIP Code) | 7b ADDRESS (City, State, and ZIP Code) |
|---|---|
| El Segundo, CA 90245 | Los Angeles Air Force Base Los Angeles, CA 90009-2960 |

| 8a. NAME OF FUNDING/SPONSORING ORGANIZATION | 8b. OFFICE SYMBOL (If applicable) | 9. PROCUREMENT INSTRUMENT IDENTIFICATION NUMBER |
|---|---|---|
| | | F04701-85-C-0086-P00019 |

| 8c. ADDRESS (City, State, and ZIP Code) | 10 SOURCE OF FUNDING NUMBERS | | | |
|---|---|---|---|---|
| | PROGRAM ELEMENT NO | PROJECT NO. | TASK NO. | WORK UNIT ACCESSION NO. |
| | | | | |

11 TITLE (Include Security Classification)
Picosecond Photoconductive Sampling Measurements of the Scattering Parameters of High-Speed Field-Effect Transistors

12. PERSONAL AUTHOR(S)
Moss, Steven C.; Smith, Duane, D.

| 13a TYPE OF REPORT | 13b. TIME COVERED FROM ___ TO ___ | 14. DATE OF REPORT (Year, Month, Day) 1988 August 22 | 15 PAGE COUNT 56 |
|---|---|---|---|

16. SUPPLEMENTARY NOTATION

| 17 | COSATI CODES | | 18 SUBJECT TERMS (Continue on reverse if necessary and identify by block number) |
|---|---|---|---|
| FIELD | GROUP | SUB-GROUP | Gallium arsenide field-effect transistor, (GaAs FET) Microwave devices, Scattering parameters, |
| | | | Photoconductive sampling Picosecond optoelectronics |

19 ABSTRACT (Continue on reverse if necessary and identify by block number)

Described are stimulus-response measurement techniques based on the photoconductive generation and sampling of picosecond electrical pulses for measuring the high-frequency scattering parameters of high-speed microwave devices. These techniques are compared with more conventional microwave diagnostic techniques.

| 20. DISTRIBUTION/AVAILABILITY OF ABSTRACT | 21. ABSTRACT SECURITY CLASSIFICATION |
|---|---|
| ☒ UNCLASSIFIED/UNLIMITED ☐ SAME AS RPT ☐ DTIC USERS | Unclassified |

| 22a NAME OF RESPONSIBLE INDIVIDUAL | 22b. TELEPHONE (Include Area Code) | 22c. OFFICE SYMBOL |
|---|---|---|
| | | |

**DD FORM 1473,** 84 MAR

83 APR edition may be used until exhausted.
All other editions are obsolete.

PREFACE

The authors gratefully acknowledge the encouragement and support of J. A. Gelbwachs and the technical assistance of M. L. Takayama.

| Accession For | |
|---|---|
| NTIS CRA&I | ☒ |
| DTIC TAB | ☐ |
| Unannounced | ☐ |
| Justification | |

By_____
Distribution/
Availability Codes

| Dist | Avail and/or Special |
|---|---|
| A-1 | |

QUALITY INSPECTED 2

## CONTENTS

FIGURES

TABLE

# I. INTRODUCTION

Recently great strides have been made in the development of wide-bandwidth microwave semiconductor devices. Devices have been constructed with bandwidths well beyond the 26-GHz bandwidth, which can be conveniently measured with modern microwave network analyzers. Consequently, one characterizes most microwave devices by measuring their scattering parameters in the dc to 26-GHz region and then extrapolating these results to higher frequencies to determine parameters of interest, such as the cutoff frequency or the maximum frequency of oscillation.[1] In this report we describe an optically based, time-domain technique for measuring the response of high-speed microwave devices. This technique is, in principle, capable of characterizing the frequency response of such devices across remarkable bandwidths (dc to 1 THz).

The development of high-speed devices has been driven by the desire to build smaller and smaller devices with a concomitant savings in weight and cost, as well as the capability to pack such smaller devices more densely onto integrated circuits. As the dimensions of devices have been reduced, the speed of response has increased. The construction of devices with submicron dimensions has resulted in devices with bandwidths in excess of 100 GHz. CaAs field-effect transistors (FETs) with quarter-micron gate lengths are commercially available with usable gain to beyond 60 GHz.[2] GaAs FETs now being constructed by electron beam lithography have gate lengths on the order of 0.1 μm.[3] These devices are expected to oscillate at much higher frequencies than conventional devices. A novel device based on a buried grating-like terminal that acts as a permeable base has been constructed by a group at MIT Lincoln Laboratories.[4] The switch-on time of this permeable-base transistor has been measured by ultrafast electro-optical sampling techniques to be approximately 5 psec.[5] Devices based on this construction have been predicted to have usable gain out to approximately 400 GHz.

A novel heterostructure device based on the resonant tunneling of charge carriers through its quantum well has been constructed by another group at MIT Lincoln Laboratories.[6] The switch-on time of this resonant tunneling diode has been measured by ultrafast electro-optical sampling techniques to be approximately 3 psec.[7] Devices based on these principles are predicted to be usable as oscillators out to 1 THz!

This discussion is not meant to be an exhaustive list of high-speed devices. However, we note that devices with a transient response of a few picoseconds have been constructed, and devices based on these same principles with response times on the order of 1 psec or less can be built in the near future, without any major advances in microfabrication techniques. Furthermore, most of the existing techniques for characterizing wide-bandwidth devices are incapable of characterizing devices with the bandwidths implied by these response times.

Techniques for characterizing high-speed microwave semiconductor devices generally fall into two categories: frequency-domain techniques and time-domain techniques. Frequency-domain measurements are usually performed with either a scalar network analyzer or a vector network analyzer. Time-domain measurements can be performed with spectrum analyzers, sampling oscilloscopes, or ultrafast optoelectronic techniques. These techniques are compatible, in that frequency-domain information can be transformed into time-domain information and vice versa via Fourier transform methods. Table 1 compares the capabilities of these various measurement techniques.[8]

Scalar network analyzers cover moderate bandwidths from 100 kHz to 40 GHz. Sets of external mixers can be added to extend this range out to 200 GHz, but only over narrow bandwidths for each set. Scalar network analyzers have a relatively small dynamic range of approximately 76 dB and a correspondingly moderate sensitivity of -60 dBm; they can yield information at offset frequencies, but they yield only amplitude, and not phase, information.

Vector network analyzers yield both amplitude and phase information. Modern network analyzers cover the frequency range from 45 MHz to 26.5 GHz. Sets of external mixers can be added to extend this range out to beyond 200 GHz, but only over narrow bandwidths for each set. These systems have a dynamic range of typically 105 dB and a sensitivity of typically -110 dBm, both larger than can be obtained with a scalar network analyzer. Vector network analyzers do not yield information at offset frequencies.

Sampling oscilloscopes that have an impulse response of approximately 25 psec are commercially available. Since they are time-domain devices, they intrinsically yield both amplitude and phase information, as well as information at offset frequencies. They have a relatively limited dynamic range of approximately 50 dB and a relatively limited sensitivity of -50 dBm. When a

6

Table 1. Comparison of Features of Stimulus-Response Measurements

| Type | Frequency Range | Dynamic Range | Sensitivity | Offset Frequency | Phase and Group Delay |
|------|-----------------|---------------|-------------|------------------|-----------------------|
| Scalar Network Analyzer | 100 kHz to 40 GHz to 200 GHz with mm-wave detectors and adapter cable | 76 dB | -60 dBm | Yes | No |
| Vector Network Analyzer | 45 MHz to 26.5 GHz (to 200 GHz with external mixers) | 105 dB | -110 dBm | No | Yes |
| Sampling Oscillo-scope | 100 kHz to 40 GHz | 50 dB | -50 dBm | Yes | Yes |
| Spectrum Analyzer | 200 Hz to 22 GHz (to 325 GHz with external mixers) | 165 dB | -115 dBm | Yes | No |
| Ultrafast Opto-electronics | 1 MHz to 1 THz | 80 dB | -60 dBm | Yes | Yes |

7

sampling oscilloscope is used as a time-domain reflectometer, substantial aberration (as much as 20% peak-to-peak) may accompany the leading edge of step inputs having these rise times.[9] Furthermore, an impedance mismatch of a few percent at the external connector to the sampling head input can greatly exacerbate these aberrations.[10]

Spectrum analyzers cover the frequency range from 200 Hz to 22 GHz. As with the vector network analyzer, their frequency range can be extended up to 325 GHz by means of sets of external mixers, with narrow frequency ranges covered by each set. Typical spectrum analyzers have a dynamic range of approximately 165 dB and a sensitivity of approximately -135 dBm. While the spectrum analyzer can provide information at offset frequencies, it cannot yield phase information.

Ultrafast optoelectronic techniques are based on the generation of ultra-fast electrical pulses by exciting photoconductive switches with ultrashort optical pulses;[11] subpicosecond electrical pulses have been generated in this manner.[12] Similarly, one can sample ultrafast electrical transients by using such a photoconductive switch as a sampling gate. Another ultrafast optoelectronic sampling technique based on the electro-optic effect has also demonstrated subpicosecond resolution.[13] Consequently, ultrafast optoelectronic techniques have a measurement bandwidth capability from near dc to greater than 1 THz. They intrinsically yield both amplitude and phase information, as well as information at offset frequencies. The dynamic range of these techniques can be as high as 80 dB, limited either by the dynamic range of the lock-in amplifier used for the measurement or by the photon or electron statistics. The sensitivity can be as high as -60 dBm, again limited by either the lock-in amplifier or the photon or electron statistics.

While it is clear that such ultrafast optoelectronic techniques have a definite advantage over the other measurement techniques in terms of frequency range and bandwidth, a more careful comparison is needed to show the advantages and disadvantages of each technique, as well as where the various techniques complement one another. Nonetheless, it is clear that at present only the ultrafast optoelectronic techniques have the frequency range and bandwidth necessary to characterize completely the high-speed semiconductor devices described above.

In the remainder of this report we describe end-to-end a system that uses the ultrafast photoconductive generation and sampling technique to characterize completely the response of high-speed GaAs FETs in terms of the scattering parameters used by microwave design engineers. In the next section we describe the experimental apparatus used in performing these measurements. We discuss the results of picosecond stimulus-response measurements on a 0.5-μm gate length Schottky-barrier GaAs FET, as well as more recent measurements on one with a 0.3-μm gate length. Also, we describe the Fourier transform methods used to convert the time-domain information to frequency-domain information and show how the scattering parameters of the device are obtained. We then assess how these results affect simple models of the frequency response of GaAs FETs. Finally, we compare in more detail the ultrafast optoelectronic technique used in these measurements with the more conventional measurement techniques, and show how the ultrafast optoelectronic techniques can be improved to yield more precise scattering parameters across broader bandwidths.

9

## II. EXPERIMENTAL TECHNIQUE AND APPARATUS

The measurements described in this report are based on the photoconductive generation and sampling of ultrashort electrical pulses developed by Auston at Bell Laboratories.[11] Picosecond electrical pulses are generated by optical illumination of the gap in a solid-state microwave waveguide, as shown in Figure 1(a). The waveguide is a microstrip line sandwiched around a silicon-on-sapphire (SOS) wafer. The gap in the microstrip exposes the thin epilayer of silicon covering the insulating sapphire. Typically, one end of the waveguide is biased at a few volts. When the gap is dark, little or no current flows across it. Illumination of the gap results in the photogeneration of electron-hole pairs, thus changing the conductivity within the gap and allowing current to flow across the gap. The duration of the electrical pulse generated is determined by the lifetime of the photogenerated charge carriers, as well as by the geometry of the gap. If the silicon epilayer is heavily ion implanted, the lifetime of the carriers may be reduced to as little as 600 femtoseconds.[14] Consequently, the duration of the photogenerated electrical pulse can be almost as short as the picosecond optical pulse.

Ultrafast photoconductive switches can also be used to sample transient electrical waveforms, as shown in Figure 1(b). If the switch is illuminated by an ultrashort optical pulse during the passage of a transient electrical waveform, current will flow across the gap for the duration of the sampling gate formed by the illumination of the switch.

The photogeneration and sampling technique applied to the measurement of the response of a two-port device is shown in Figure 2. A high-speed device is placed between two waveguides, each of which has two ultrafast photoconductive switches. The bias of the device is controlled by each of the central microstrips. Biasing one of the side microstrips allows the bias of the device to be modulated by means of the illumination of the ultrafast switch by an ultrashort optical pulse. The ultrafast transient thus generated on the central microstrip propagates along the central microstrip to the device, where part of the transient waveform is reflected and part is transmitted. The reflected waveform can be sampled at the other switch on the same side of the device, while the transmitted waveform can be sampled at either of
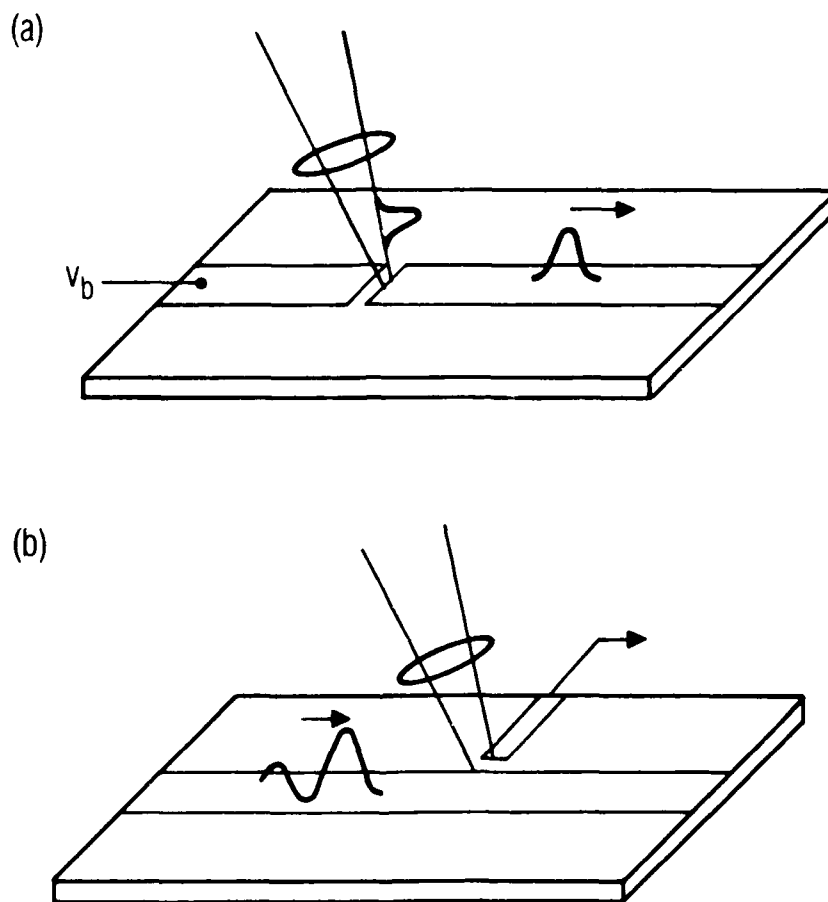
11

(a)

$V_b$

(b)

Figure 1.  (a) Photoconductive Generation of Picosecond Electrical Pulses and
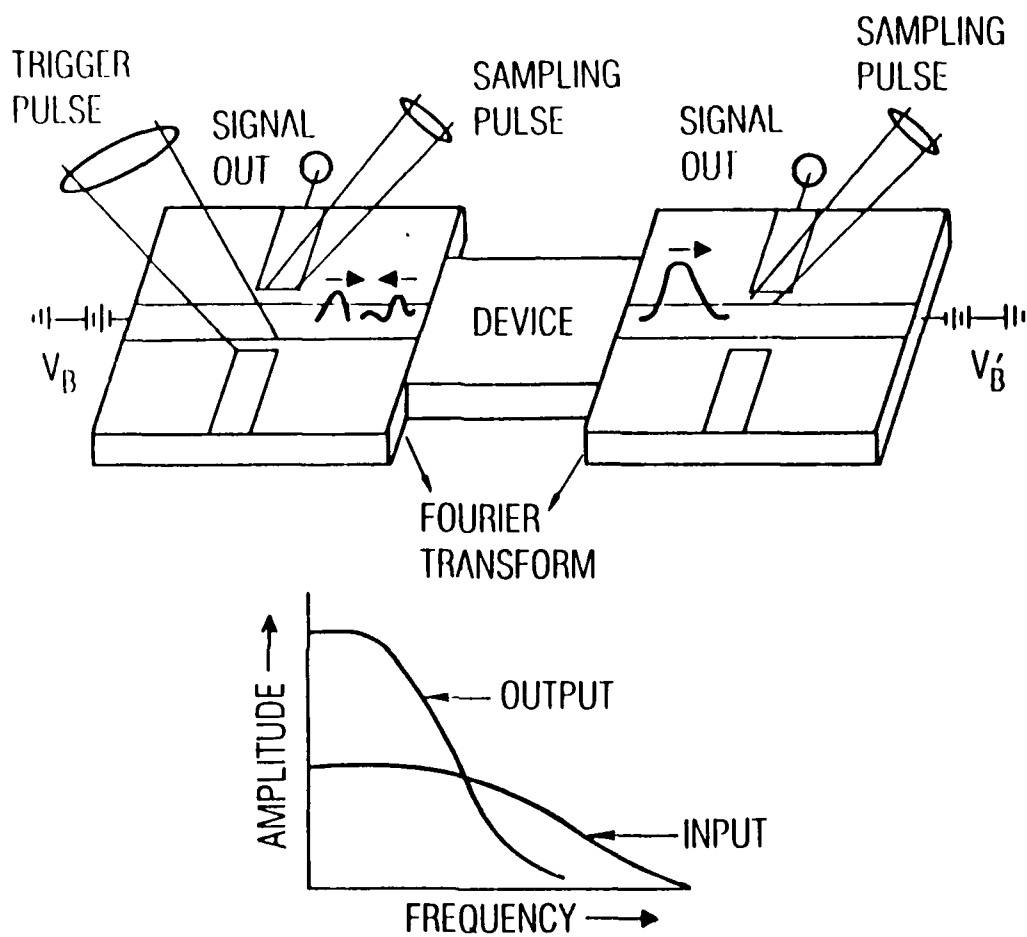(b) Photoconductive Sampling of Picosecond Electrical Transients.

12

Figure 2.   Picosecond Optoelectronic Pulse-Response Measurement Technique.

the switches on the other side of the device. Since any switch can be used either to generate or to sample electrical transients, we can measure the reflected signals on both sides of the device as well as the signals transmitted through the device in each direction. The bias levels applied to the device ports are independently controlled, so that these measurements can be performed at any device bias desired. By controlling the optical intensity at the photogeneration switch, one can control the amplitude of the transient electrical waveform. Consequently, this technique allows one to determine both the small-signal and large-signal response of the device. Finally, while the measurements described here are on a GaAs FET configured as a two-port device, the technique is adaptable to multiport devices.

The temporal responses of the devices measured were obtained by the picosecond pump and probe technique, which is the optical analog of sequential equivalent time sampling used in some sampling oscilloscopes to reconstruct high-speed waveforms.[15] A schematic diagram of the technique is shown in Figure 3. A picosecond optical pulse is split into two parts at a beam-splitter. One part is directed along a fixed path onto an ultrafast photo-conductive switch, thus generating an ultrafast transient electrical wave-form. The other part is directed along a path of variable length controlled by the position of a mechanical translation stage. This pulse is then directed onto a second ultrafast photoconductive switch, thereby producing the sampling gate. The length of the variable path can be controlled so that the sampling gate can be produced before, during, and for hundreds of picoseconds after the generation of the ultrafast electrical waveform.

Two different systems were used to perform these measurements. The system used on the 0.5-µm gate-length GaAs FET is shown in Figure 4.[16] A train of picosecond optical pulses was produced by a dye laser synchronously pumped by an actively mode-locked argon-ion laser. The average output power of the dye laser was maximized by adjustment of a three-plate birefringent tuning element. A crossed-beam second-harmonic autocorrelation technique measured the temporal pulsewidth of the dye laser pulses to be approximately 4 psec. The period between pulses in the train was approximately 4.3 nsec. Total dye-laser average power was approximately 100 mW. The pulse train was split into two parts, and each part was directed separately onto ultrafast photoconductive switches located in our test fixture. The pulse generation
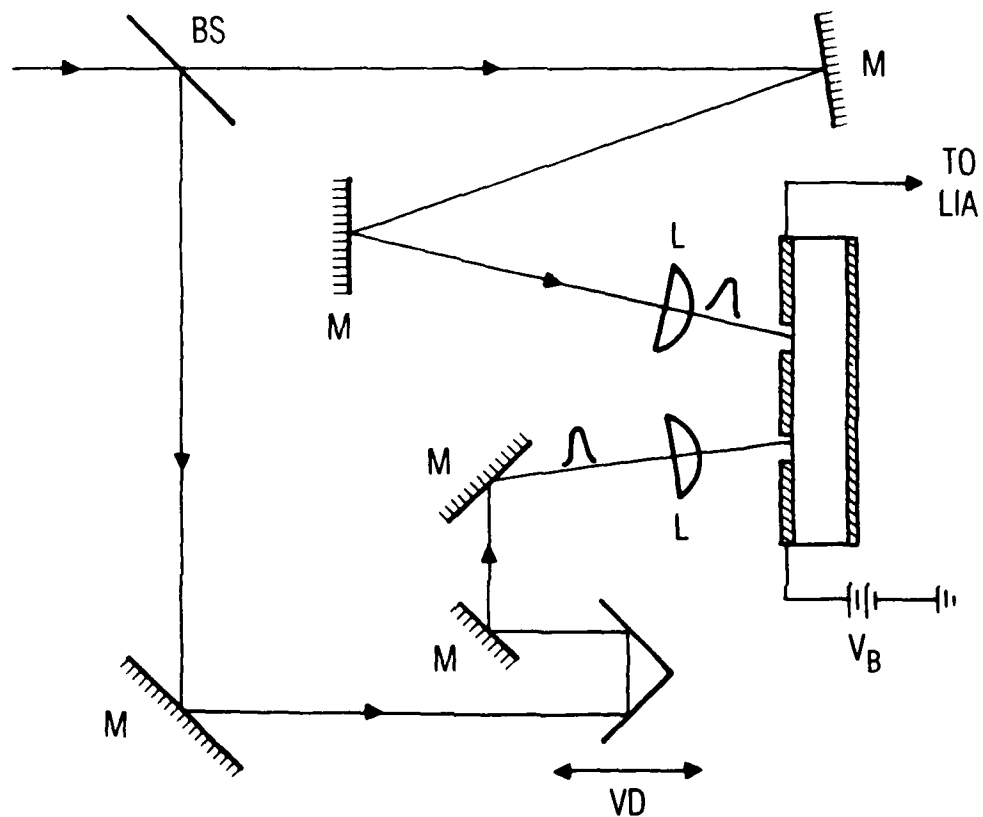
Figure 3.   Optical Excite-and-Probe Technique.   (M - mirror, BS - beam-
splitter, L - lens, LIA - lock-in amplifier, $V_B$ - applied bias
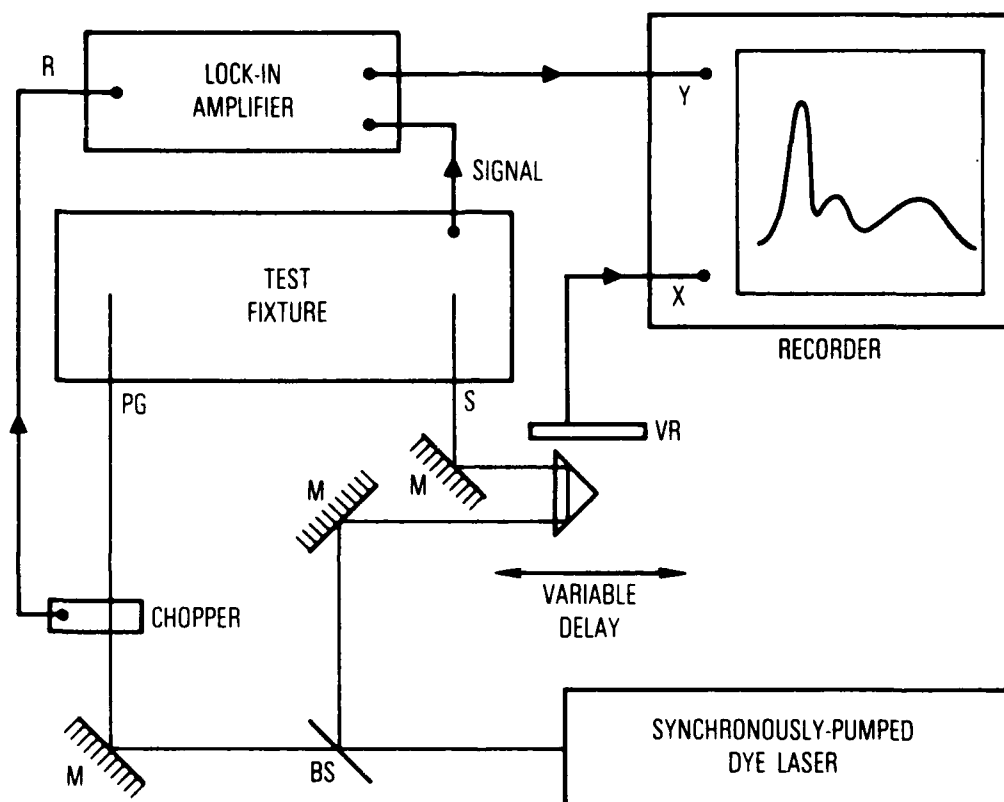voltage, VD - variable temporal delay.)

Figure 4.  Early Experimental Apparatus.  (R - references, M - mirror, BS - beam-splitter, PG - pulse generator, S - pulse sampler, VR - voltage ramp.)

and sampling were done with the ultrafast photoconductive switches and device arranged as shown in Figure 3. The transient response of the device was measured by the picosecond pump and probe technique described above. A mechanical chopper was inserted into the fixed beam-path to provide a reference for the signal taken from the sampling aperture to the lock-in amplifier. The fixed beam-path was mechanically chopped at 808 Hz with a 50% duty cycle. The laser fluence at each switch was approximately 15 $\mu J/cm^2$. The mechanical translation stage allowed 8.3 cm of travel. The output of the lock-in amplifier was fed into the y-axis input of an x-y recorder. The x-axis input was obtained from a voltage ramp controlled by the position of the translation stage. The voltage ramp was provided by a resistive strip positioned on the stationary part of the translation stage. One end of the resistive strip was biased at +5 V. A wiper blade attached to the moving part of the translation stage provided a traveling contact that functioned as a voltage divider, thus providing a sensitive measurement of the output of the test fixture as a function of time delay between generating and sampling pulses. This voltage ramp system was limited to a temporal resolution of approximately 1 psec, primarily because of the width of the contact region between the wiper and the resistive strip. Smaller contacts were too sensitive to jitter caused by friction between the wiper and the resistive strip. The data were digitized by a magnetostrictive digitizer attached to a microcomputer prior to the analysis; the fast Fourier-transform techniques described later in this report were used.

The system used to perform measurements on the 0.3-$\mu$m gate-length GaAs FET is shown in Figure 5. A train of picosecond pulses is produced by a dye laser synchronously pumped by the doubled frequency output of an actively mode-locked Nd:YAG laser. Nd:YAG laser pulses as short as 60 psec are obtained by the second-harmonic mode-locking technique.[17] A crossed-beam second-harmonic autocorrelation technique measured the temporal duration of the dye-laser pulses to be approximately 2 psec. The period between pulses in the pulse train was approximately 10 nsec. Total dye-laser average power was approximately 65 mW. The generation and sampling of the picosecond electrical pulses were performed as described above. The transient-response measurements were performed on the device by the picosecond pump and probe technique described above. The beam used to generate the picosecond electrical transients on our test fixture was modulated by an acousto-optic modulator
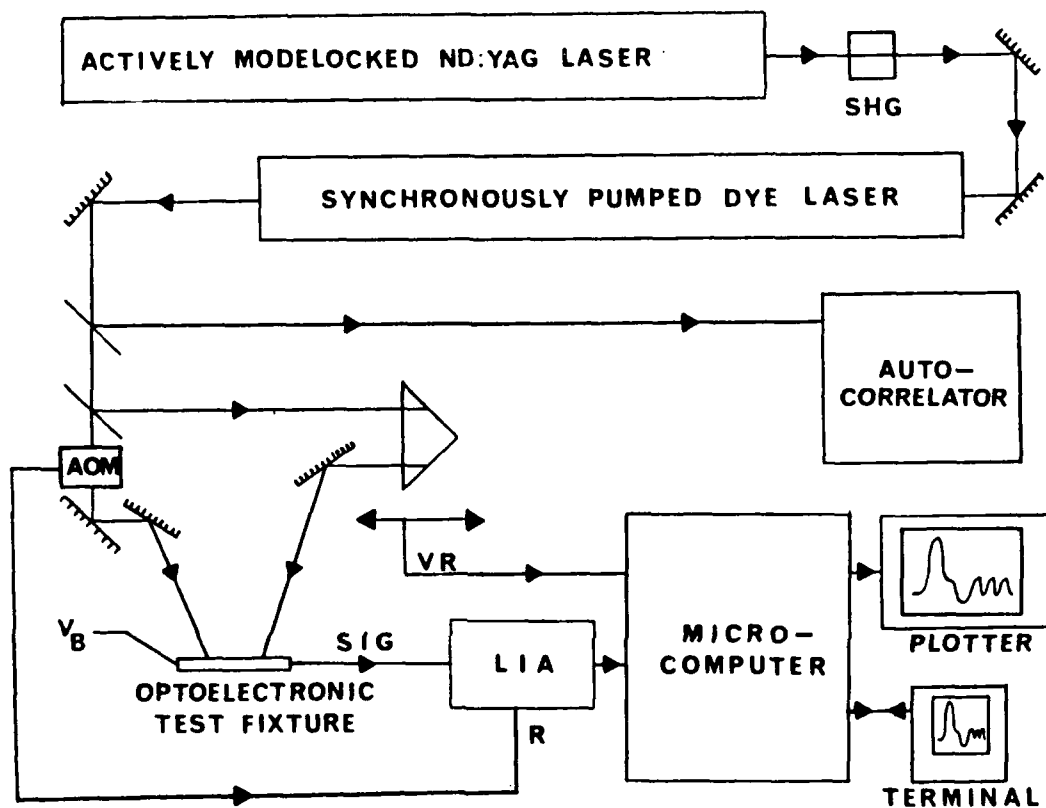
Figure 5. Latest Experimental Apparatus. (SHG – second-harmonic generator, M – mirror, BS – beam-splitter, LIA – lock-in amplifier, VR – voltage ramp, AOM – acousto-optic modulator, LIA – lock-in amplifier.)

driven at 1 kHz; the zeroth-order beam had a 70% depth of modulation. The phase noise inherent in these modulation techniques was reduced by more than an order of magnitude from that observed when the mechanical chopper was used as the modulator. The signal from the sampling aperture was taken to a lock-in amplifier referenced to the modulation frequency of the acousto-optic modulator. The laser fluence at each switch was approximately the same as described above. The translation stage used to vary the path length traversed by the sampling beam was the same as described above. The output of the lock-in amplifier was fed through an A/D converter into a microcomputer. The voltage ramp, controlled by the position of the translation stage, was fed through a second A/D converter into a microcompurer. The waveform obtained by this sequential equivalent time-sampling technique was displayed on a monitor and constantly updated, as averaging occurred during several scans of delay. This arrangement provided a very sensitive measurement of the output of the test fixture as a function of time delay between generating and sampling pulses, and it also avoided the need for the tedious digitization procedure required previously.

We applied this technique to determine the impulse response of unpackaged GaAs FETs, each of which was embedded in one of two different test fixtures, as shown in Figure 6. Measurements were performed on a Schottky-barrier GaAs FET with a 0.5-μm-long gate (Avantek AT-8041) designed as a wideband, low-noise amplifier for the 10 to 26-GHz region, and on a Schottky-barrier GaAs FET with a 0.3-μm-long gate designed as a low-noise preamplifier for the 18 to 45-GHz region. Photoconductive generators and samplers were fabricated in microstrip transmission lines on SOS substrates. The gold microstrips were 1500 Å thick, with a 50-Å layer of chromium between the gold microstrip and the silicon to facilitate the bonding of the gold to the silicon. The test fixtures were ion implanted (with either $10^{15}$ $O^+$ per $cm^2$ at 400 keV or $10^{15}$ $Si^+$ per $cm^2$ at 400 keV) to allow the generation of 5 to 7-psec electrical pulses. The temporal width of the electrical pulses produced depends on the temporal width of the optical pulses, the geometry of the switch, and the lifetime of the carriers generated in the photoconductive material in the gap. In these measurements the temporal width of our optical pulses is short enough (2 to 4 psec) that the temporal width of the electrical pulses is dominated by the lifetime of the photogenerated carriers and the geometry of the switch. Thus, even with subpicosecond optical pulses, we would be limited
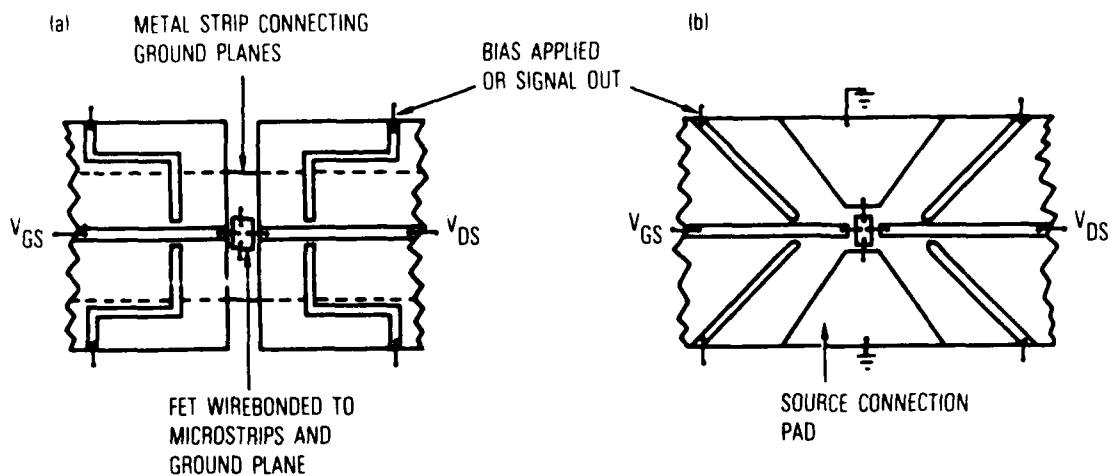
Figure 6. FET Wire-Bonded into Test Fixtures. (a) Split test fixture.
(b) Planar test fixture. $V_{GS}$ - applied bias potential
between gate and source; $V_{DS}$ - applied bias potential
between drain and source.

to approximately 4-psec electrical pulses. Each test fixture had two central microstrips (one on each side of the device) to control the operating point of the FET, and four side microstrips (two on each side of the device) to allow the various reflection and transmission coefficients (scattering parameters) for this two-port device to be monitored. The electrical pulses were generated by illumination of the 25-μm gap between the central microstrips and one of the side microstrips, which was biased at +40 V. The electrical pulses were sampled by illumination of the 25-μm gap between the central microstrips and one of the other side microstrips.

In the split fixture [Figure 6(a)] two separate SOS wafers were connected by a single gold-plated Kovar strip attached to each ground plane with conductive epoxy (Epotek H20E). The SOS wafers were 180 μm thick, while the photoconductive layer of silicon was either 0.5 or 1.0 μm thick. The thinner epilayer produced shorter electrical pulses, primarily because the ion implantation process produced damage more uniformly through the epilayer. The FET was epoxied into the approximately 1-mm gap between the SOS wafers and onto the Kovar plate below. The gate and drain pads of the FET were wire-bonded to the central microstrips on each side of the device, while the source pads were wire-bonded to the Kovar ground plane. The microstrips were 180 μm wide, with a 50-ohm impedance and a low-frequency effective dielectric constant of 6.65.

The planar fixture design [Figure 6(b)] was used to simplify fixture fabrication and reduce the inductance of the source bond wires. This design was fabricated on a single SOS wafer. The SOS wafer was 250 μm thick, while the photoconducting layer of the silicon was 1 μm thick. The FET was epoxied into the gap between the two central microstrips. Again, the gate and drain pads were wire-bonded to the central microstrips. In this fixture, however, the source pads were wire-bonded to two relatively low-impedance, trapezoidal gold pads. Furthermore, the ends of the side microstrips forming the gaps with the central microstrip were rounded to prevent the relatively large edge effects observed in the split fixture. The microstrips were 250 μm wide to yield low-frequency microstrip parameters that were the same as those for the other fixture. The 0.5-μm-gate GaAs FET bonded into the planar test fixture is shown in Figure 7.
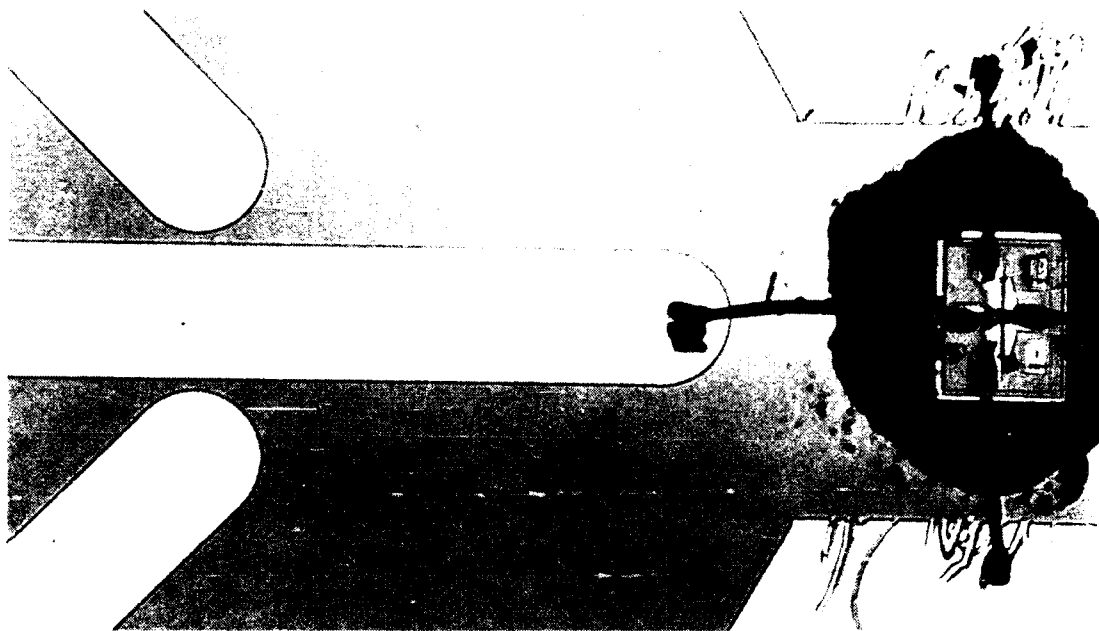
Figure 7.   Photograph of Avantek AT-8041 (0.5-μm-Gate Schottky-Barrier GaAs
FET) Wire-Bonded into Planar Test Fixture.

The test fixtures were placed into brass fixture holders that had SMA bulkhead connectors at the appropriate locations to make electrical connection with each of the central and side microstrips. The central conductor of the SMA connectors was connected to the microstrips by a high-conductivity silver paint (Dotite). The ground plane of the test fixture was connected to the brass fixture holder by the same silver paint. The outer conductor of the SMA connectors was held at ground and was in contact with the brass fixture holder.

In each fixture the operating point of the FET was controlled by dc voltages applied to the gate and drain microstrips. Furthermore, the absolute magnitude of the input and output electrical signals was determined by referencing the measured signal levels to those obtained with a 10-mV square wave on the central microstrip.

# III. TEMPORAL RESULTS

The pulse response of the 0.5-μm-gate Schottky-barrier GaAs FET (Avantek AT-8041) in the split fixture is shown in Figure 8. These measurements were performed with a drain-to-source voltage of 3.0 V and a drain current of 30 mA. Figures 8(a) and (d) were produced from measurements of the reflection at the gate and drain side of the device, respectively. For these measurements the pulses are generated at one port of the device and sampling is done at the same port immediately opposite the pulse-generation switch. Thus the large initial peak, approximately 10 psec wide (FWHM), represents the profile of the pulse as it is generated, and corresponds to an optoelectronic autocorrelation measurement. The shoulder on the trailing edge of the pulse profile is caused by a reflection at the wire bond of the microstrip. The broad signal at later times is due to the reflection from the FET and contains the information about the device's response. Finally, the reflection measurements show an oscillatory signal at even later times; we attribute this to reflections from the right-angle bends within the side microstrip circuitry.

Figure 8(b) shows the results of injecting a signal on the drain side and sampling the gate response. The complicated features reflect the fact that the gate is capacitively coupled to the rest of the transistor.

Figure 8(c) shows the result of amplifying a signal by injecting it on the gate side and sampling on the drain side. The signal is increased in amplitude over the input signal and broadened temporally to about 25 psec (FWHM), which demonstrates the limited frequency respons of the FET. The shape of all of the signals resulting from either reflection off the FET or transmission through the FET varies with the bias voltages and currents, which indicates that signals are affected by variations in device capacitances and transconductances.

The pulse response of a 0.5-μm-gate Schottky-barrier GaAs FET in the planar test fixture is shown in Figure 9. As with the split fixture, all of the measurements were performed with the drain-to-source voltage set at 3.0 V and a drain current of 30 mA. Again, Figures 9(a) and (d) show the reflection off the gate and drain side of the device, respectively, while Figure 9(b) shows the pulse injected at the drain port and sampled at the gate port, and Figure 9(c) shows a pulse amplified after being injected on the gate side and

Figure 8.  Pulse Response of 0.5-μm-Gate FET in Split Test Fixture.  (a) Pulse and sample gate side; (b) pulse drain side, sample gate side; (c) pulse gate side, sample drain side; (d) pulse and sample drain side.
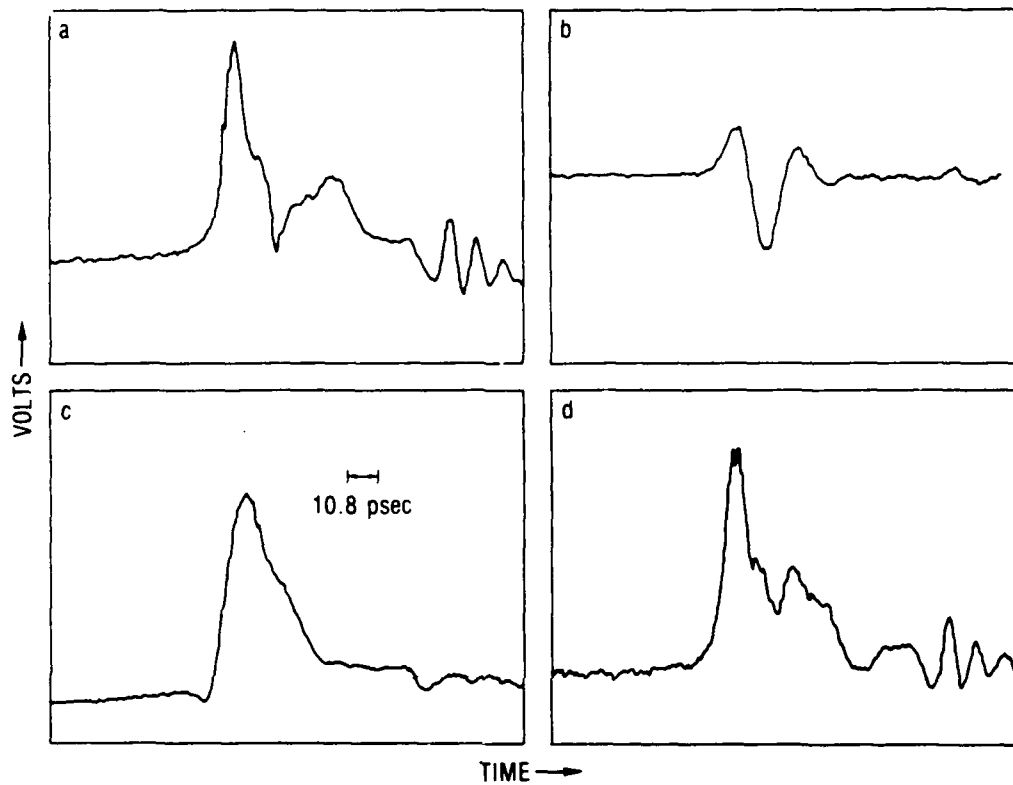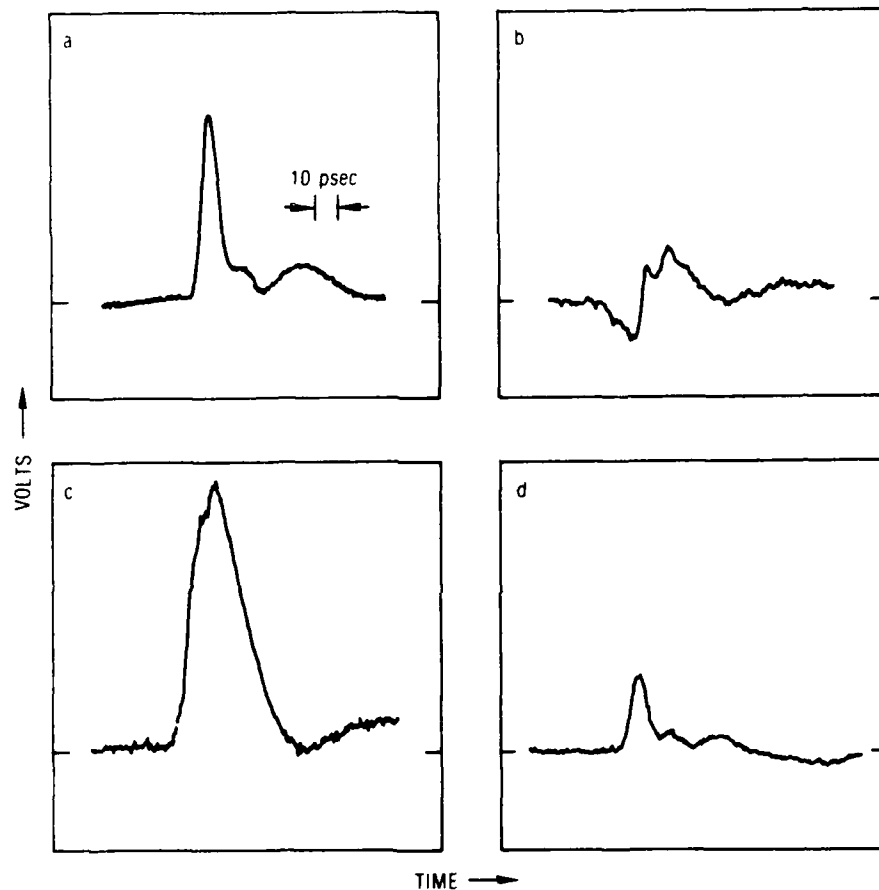
Figure 9.   Pulse Response of 0.5-μm-Gate FET in Planar Test Fixture.
(a) Pulse and sample gate side; (b) pulse drain side, sample gate
side; (c) pulse gate side, sample drain side; (d) pulse and sample
drain side.   $V_{DS} = 3.0$ V, $I_{DS} = 30$ mA.

sampled on the drain side. The duration of the optoelectronic autocorrelation was again approximately 10 psec (FWHM). The amplified pulse transmitted from the gate to the drain side of the FET was 1.5 times the peak amplitude of the input pulse and was broadened to a width of approximately 25 psec.

In comparing Figures 8 and 9, notice first that the shoulder on the autocorrelation peak in the (a) and (d) parts is better resolved in the planar test fixture because there is a longer section of microstrip between the photoconductive switches and the wire bond. Second, the oscillatory artifact present in the reflection measurements with the split test fixture is absent in the reflection measurements with the planar test fixture. This is because the side microstrips on the planar test fixture were straightened. These improvements in the test fixture design make the data much easier to analyze.

In comparing Figures 8(c) and 9(c) we see that the rise time of the amplified pulse was shorter in the split fixture, with an 8.2-psec rise time compared to the 15-psec rise time in the planar fixture. The 8.2-psec rise time of the FET in the split fixture is the fastest temporally resolved FET rise time of which we are aware. We attribute the difference in rise times to the difference in length of the source bond wires in each fixture. The source bond wires in the split test fixture were relatively long (approximately 1 mm) compared to the source bond wires in the planar test fixture, which were only approximately 350 μm long. The inductance associated with the longer source bond wires in the split test fixture may have reduced the gain and contributed a high-frequency resonance to produce this very rapid rise time.

Figure 10 displays a complete set of measurements of the temporal response of the 0.5-μm-gate FET in the planar test fixture, but with no bias applied to the gate or drain of the FET. The reflection measurements shown in Figures 10(a) and (d) are very similar to the results shown in Figures 9(a) and (d), where bias was applied to the device. The gate-side reflection of the FET is temporally shorter with applied bias corresponding to the smaller gate-source capacitance (a result of the increased size of the depletion region under the gate). Similar effects are observed in the reflection on the drain side, shown in Figures 9(d) and 10(d). With no bias applied the signal transmitted from the gate to the drain side of the device shown in Figure 10(c) is not amplified and merely displays the capacitive coupling between the gate and the rest of the FET.
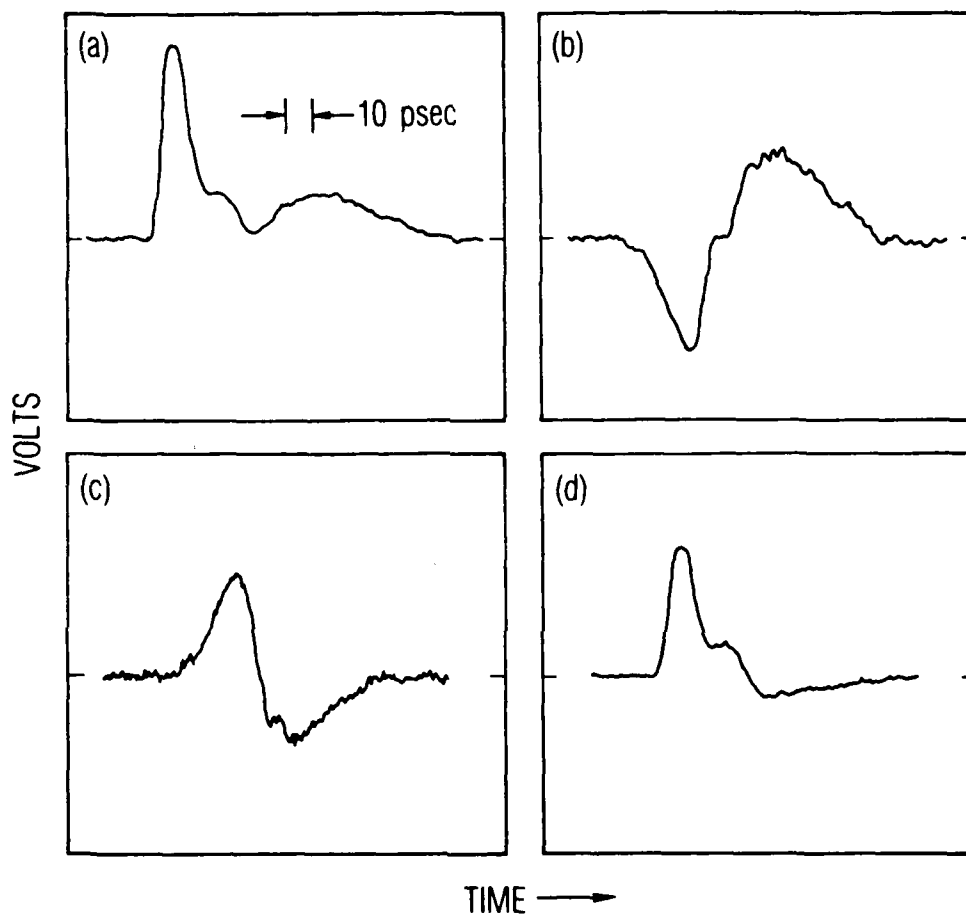
Figure 10. Pulse Response of 0.5-μm-Gate FET in Planar Test Fixture, with No
Bias Applied to Gate or Drain. (a) Pulse and sample gate side;
(b) pulse drain side, sample gate side; (c) pulse gate side, sample
drain side; (d) pulse and sample drain side.

The effects of bias on the pulse transmitted from the drain to the gate are displayed in Figure 11. These measurements were the most difficult to perform, since the FET does not readily transmit in this direction and the losses on passage through the wire bonds and the FET itself were substantial. The transmitted waveforms are severely broadened and distorted. After excitation with a 7-psec electrical transient, the FET requires around 80 psec to recover. In each case the initial polarity of the waveform is opposite to the input polarity. The transient waveform measured at the gate decreases nearly monotonically for 30 psec, then abruptly reverses polarity. With no bias applied to the FET [Figure 11(a)], the response returns to zero within a few picoseconds and remains quiescent for a few picoseconds before reversing polarity. With bias applied to the FET [Figures 11(b) and (c)], the waveforms reverse polarity within 5 psec and display a complicated oscillatory behavior over a time scale of tens of picoseconds. These features qualitatively display the capacitive coupling at the gate, which inverts and differentiates the signal incident on it from the drain side. Additionally, the transmitted signal is stretched temporally, and corresponds to the limited bandwidth of the FET. The similarity of these measurements indicates that the device's response is dominated by features independent of electrical bias, e.g., the impedances associated with coupling the FET to the test fixture.

We have performed a preliminary set of measurements of the response of a 0.3-$\mu$m-gate Schottky-barrier GaAs FET embedded in a split test fixture. Figures 12(a) and (b) display the transient reflection on the gate side of the device for two bias conditions. Figures 12(c) and (d) display the transient signal transmitted from the gate side of the GaAs FET to the drain side under the same two bias conditions. Figures 12(a) and (c) were obtained with the FET biased at $V_{DS} = 0.3$ V and $V_{GS} = 0.45$ V. Figures 12(b) and (d) were obtained with no bias applied to the gate or drain of the FET. The differences observed in these preliminary measurements are only partially due to the different bias conditions. Figures 12(b) and (d) were obtained with a GaAs FET embedded in a different test fixture than the GaAs FET for which the results of Figures 12(a) and (c) were obtained. That is, for the results shown in Figures 12(b) and (d), the SOS wafers on which the waveguides were fabricated were thinner (180 $\mu$m), with correspondingly narrower microstrip widths (to maintain 50-ohm impedance). Consequently, the electrical pulses

30
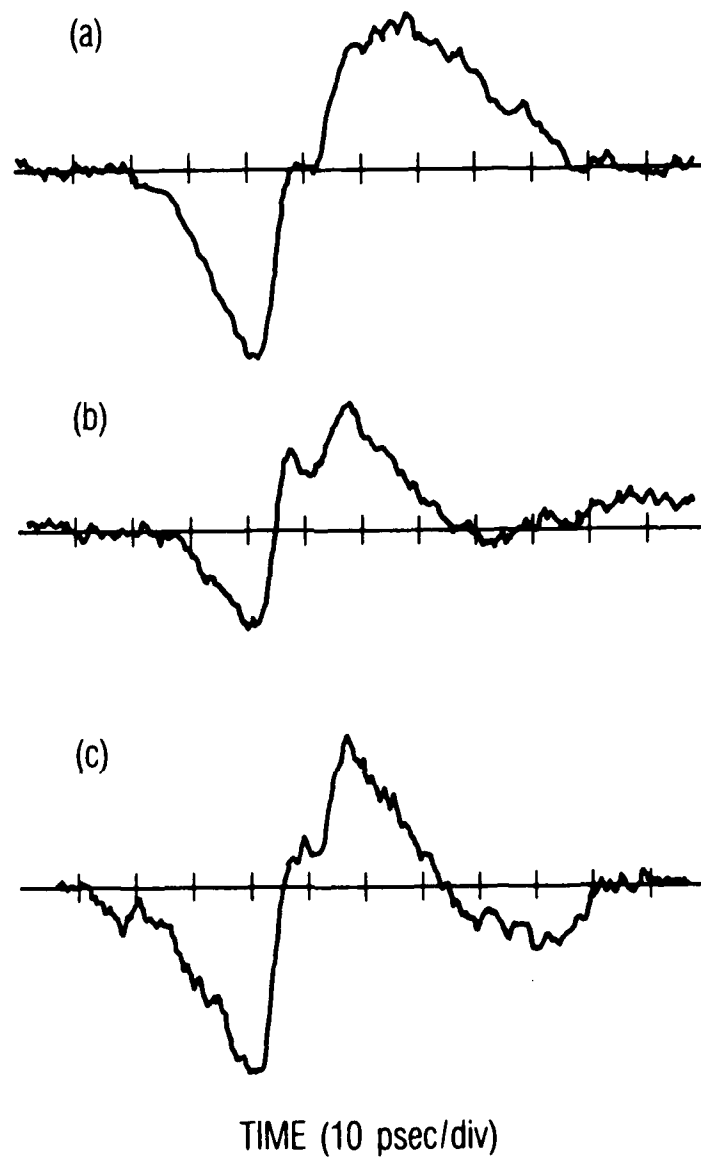
Figure 11. Pulse Drain Side, Sample Gate Side of 0.5-μm-Gate FET in Planar
Test Fixture. (a) No applied bias; (b) $V_{DS} = 3.0$ V, $I_{DS} = 30$ mA;
(c) $V_{DS} = 3.0$ V, $I_{DS} = 8$ mA.

31
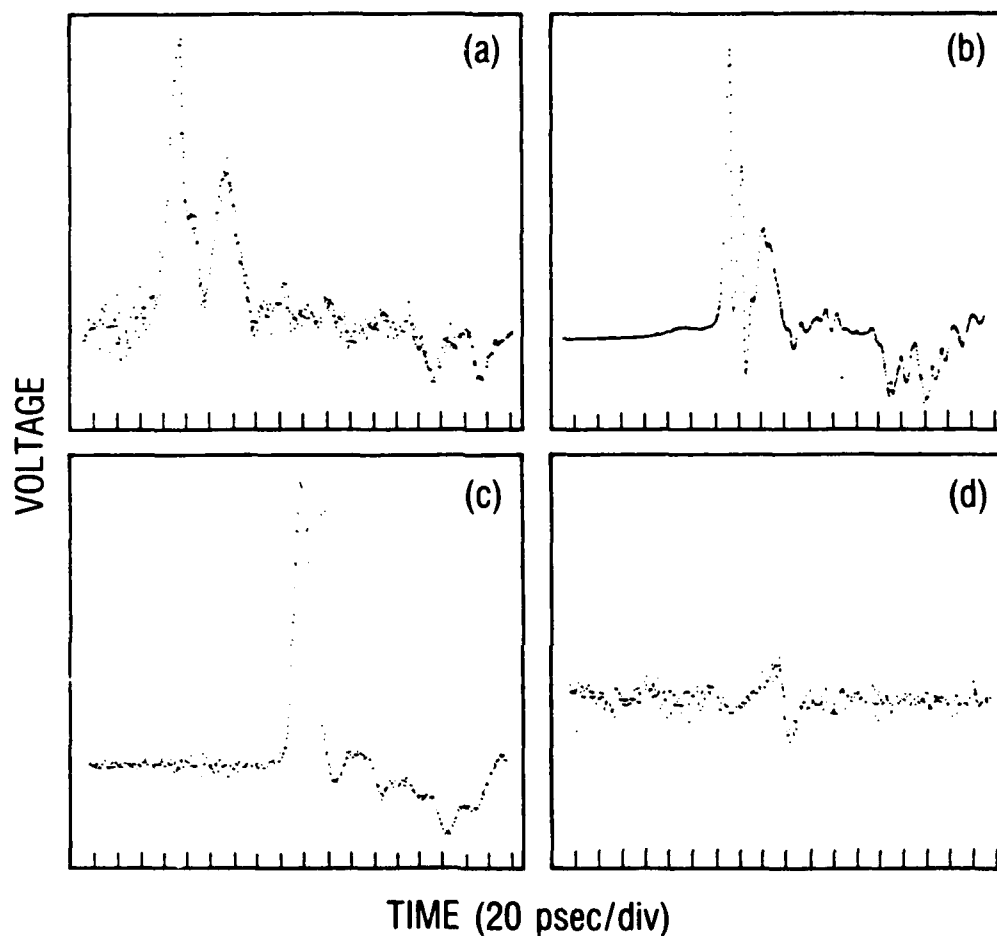
Figure 12. Pulse Response of 0.3-μm-Gate FET in Split Test Fixtures. (a) and (b) Pulse and sample gate; (c) and (d) pulse gate, sample drain; (a) and (c) with the FET biased at $V_{DS}$ = 3.0 V and $V_{GS}$ = -0.45 V; (b) and (d) with no bias applied to the gate or drain of the FET.

produced were shorter, as one can clearly see by comparing Figures 12(a) and (b). With the shorter pulses, the optoelectronic autocorrelation is almost completely distinct from the reflection at the wire bond in Figure 12(b). Furthermore, note that the reflection at the wire bond is much more complicated than that displayed in the measurements on the 0.5-μm-gate FET, with both positive and negative polarity indicating a complex resonance. Finally, the signal injected at the gate, amplified, and sampled on the drain side [Figure 12(c)] is broadened to only 17 psec (FWHM) by its passage through this device; this is much less than the corresponding signals amplified by the 0.5-μm-gate FETs, and is consistent with the much larger bandwidth of the 0.3-μm-gate FET. With no bias applied to the device, there is no gain and no active interaction with the FET. Consequently, the signal transmitted through the device [Figure 12(d)] displays only the capacitive coupling of the gate to the rest of the FET.

Finally, this device displayed virtually no gain under bias. The I-V characteristics of the device, measured by a Tektronix circuit tester and displayed in Figure 13, show that the device does not pinch off until nearly -4.0 V are applied to the gate, compared with the specified pinch-off voltage of -1.5 V. This behavior is consistent with a measured ideality factor of approximately 1.4 and implies contamination of the channel region underneath the gate. This device was a prototype obtained from Avantek. Later versions of this device have been fabricated by other processing technologies that have apparently avoided these problems.
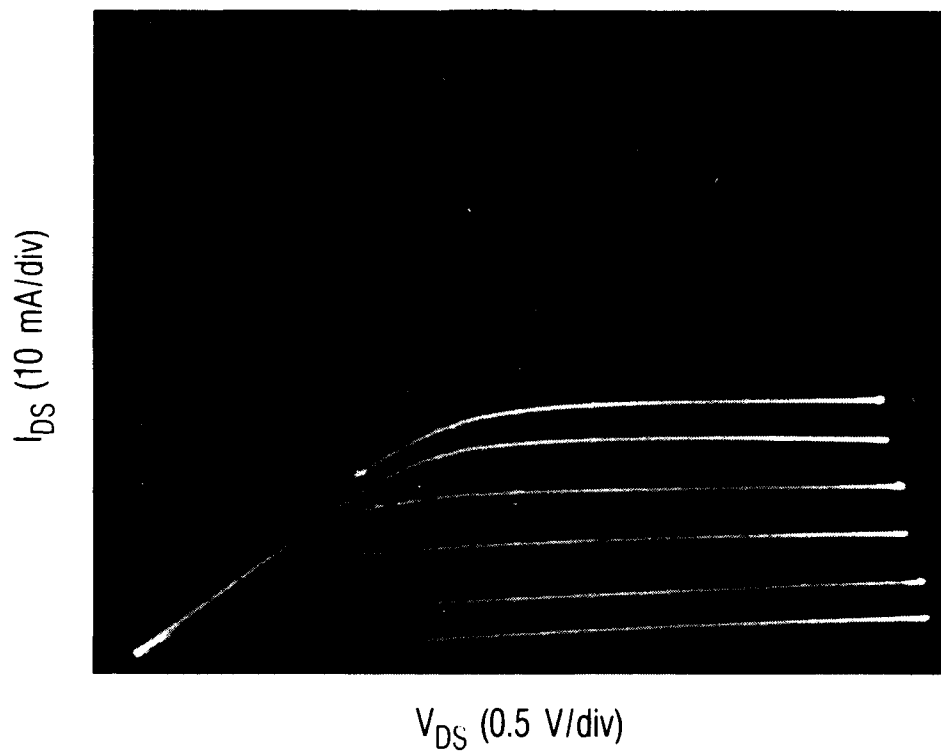
33

Figure 13. Current-Voltage Characteristics of 0.3-μm-Gate FET in Split Test
Fixture.  Gate bias varied in 0.5-V steps.

# IV. FREQUENCY-DOMAIN RESULTS

The analysis of the time-domain data to recover the frequency-domain scattering parameters followed the methods developed for purely electronic time-domain measurements. The waveforms measured by the 0.5-μm-gate GaAs FET were digitized by a magnetostrictive digitizer connected to a microcomputer at 256 points along each waveform. All of the waveforms measured by the 0.3-μm-gate GaAs FET were fed from the lock-in amplifier directly to an A/D converter connected to a microcomputer. A fast Fourier transform was used to convert the time-domain information to the frequency domain. The spacing between points in the time-domain data was approximately 1.055 psec for the waveforms of the 0.5-μm-gate FET, and approximately 0.68 psec for the waveforms associated with the 0.3-μm-gate FET. Consequently, the frequency spectrum associated with response of the 0.5-μm-gate FET consisted of 129 points, each separated by approximately 3.7 GHz, beginning at 0.0 GHz. The frequency spectrum associated with the response of the 0.3-μm-gate FET consisted of 257 points, each separated by approximately 2.9 GHz, beginning at 0.0 GHz. In each case the temporal spacing is small enough to prevent aliasing.[18] Also in each case, the spectrum drops to noise levels well before the end of its range. Finally, the data were normalized to correct for the different widths of the input pulse and the sampling aperture. The spectra of the reflected signals were normalized by simply dividing by the corresponding spectrum of the waveform of the input pulse. The spectra of the transmitted signals were normalized by dividing by the harmonic mean of the spectra obtained from input pulses on both sides of the device. The harmonic mean was then normalized to the amplitude of the appropriate input.

While this procedure accounts for the possibility that switches separated by a considerable distance may have different temporal responses, it does not account for the possibility that generating and sampling switches on the same side of the device may have different responses. This possibility may be tested, however, by generating and sampling pulses at each switch in turn and comparing the results. The result of this data analysis is the frequency spectrum of one of the four scattering parameters. $S_{11}$ is derived from the reflection of a pulse off the gate [Figures 8(a), 9(a), 10(a), and 12(a) and (b)], and $S_{22}$ is derived froam the reflection of a pulse off the drain [Figures 8(d), 9(d), and 10(d)]. $S_{21}$ and $S_{12}$ are measured by passing a pulse

35

from the gate to the drain [Figures 8(c), 9(c), 10(c), and 12(c) and (d)] and vice versa [Figures 8(b), 9(b), 10(b), and 11(a), (b) and (c)]. Thus the device can be completely characterized by these four stimulus-response measurements.

The response of the normalized FET is a complex function of the frequency (see Figure 14) and thus contains both amplitude and phase information. The magnitude of the normalized FET is the gain or reflection coefficient. The phase angle is also an important parameter to measure, and a discussion of the determination of the phase factors illustrates the ease with which de-embedding can be done with the picosecond optoelectronic technique. In a Fourier transformation a temporal delay transforms into a phase shift with frequency, and thus quantitative measurement of the phase factors requires determination of the temporal origin of the time-domain waveforms. As can be seen in Figures 8(a), 9(a), 10(a), and 12(a) and (b), the temporal origin is clearly marked by the optoelectronic autocorrelation peak. Using this peak as the temporal origin fixes the reference plane at the optoelectronic switches. Subtracting this peak from the waveform yields the pulse response for a system consisting of a short length of microstrip, a bond wire, and the FET connected to the rest of the circuit. Since the trailing edge of the optoelectronic autocorrelation peak overlaps temporally with the leading edge of the reflection from the wire bond, we must approximate the shape of the autocorrelation in this region in order to subtract it from the signal. We estimate that the errors inherent in this approximation may be as large as 20% at 70 GHz, and larger at higher frequencies. Clearly, shorter pulses that cleanly separate the autocorrelation from the reflection at the wire bond are an advantage here. Ideally, one would like to measure the pulse response of the FET alone, and the de-embedding process consists of measurements and data manipulation intended to eliminate mathematically the effects of the other components.

In our measurements we approximate the microstrip as a dispersionless transmission line that adds only a propagation delay to the time-domain data. The propagation constant of the microstrip is measured in a separate experiment,[19] and the temporal origin of the waveform is shifted to compensate for the approximate length of microstrip. Thus, the effects of the microstrip are mathematically removed and the reference plane is moved up to the micro-
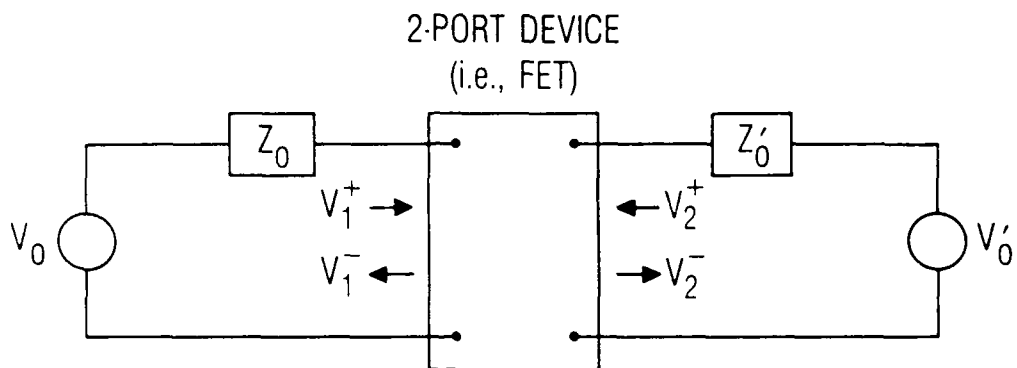
2-PORT DEVICE
(i.e., FET)

$$V_1^- = S_{11}V_1^+ + S_{12}V_2^+$$
$$V_2^- = S_{21}V_1^+ + S_{22}V_2^+$$

S MATRIX IS COMPLEX AND FREQUENCY-DEPENDENT

Figure 14. Two-Port Device Characterization in Terms of Scattering Parameters.

strip/wire-bond interface. The same temporal origin (corresponding to a position of the optical delay line) was used for the calculation of all four scattering parameters.

Additional data manipulation can be performed through time-domain windowing.[20] This process removes waveform regions that are identified with electrical components other than the device under test. An example is the subtraction of the autocorrelation peak from the reflection waveforms. Caution must be exercised when using the windowing technique or when subtracting one feature, such as the optoelectronic autocorrelation, from the data. A waveform identified as a spurious reflection may obscure part of the signal of interest or deform it so that cleanly separating the spurious reflection from the signal of interest may be difficult (as in the case of separating the optoelectronic autocorrelation from the reflection at the wire bond). This technique could also be applied to the microstrip/wire-bond reflection, since it is unrelated to the FET itself. However, the pulses reflected from the FET must pass through this interface; thus windowing of this reflection would not remove all the effects of the interface. Furthermore, we wished to reproduce as nearly as possible the measurements performed by the manufacturer, which include this interface. A better technique for de-embedding the wire bond would be to characterize a wire bond of the same length that connects the microstrip to the ground plane. In any case, the picosecond optoelectronic technique leads to very simple de-embedding procedures and is particularly suited to time-domain windowing.

Figure 15 is a Bode plot of the $S_{21}$ scattering parameter of the 0.5-$\mu$m-gate FET in the split test fixture. For these measurements the voltage amplitudes of the waveforms were not adequately calibrated. Consequently, we present here only relative amplitudes. This means we cannot determine the cutoff frequency of the device. Nonetheless, information about the device's frequency response is available. For example, at frequencies beyond 10 GHz the insertion-gain spectrum falls off as the inverse of the frequency, which is as expected.

Figure 16 shows the scattering parameters calculated from the pulse response of the FET in the planar test fixture. The manufacturer's scattering parameters (measured by conventional means) are also shown, although the two sets of data are not directly comparable because of the different test

38
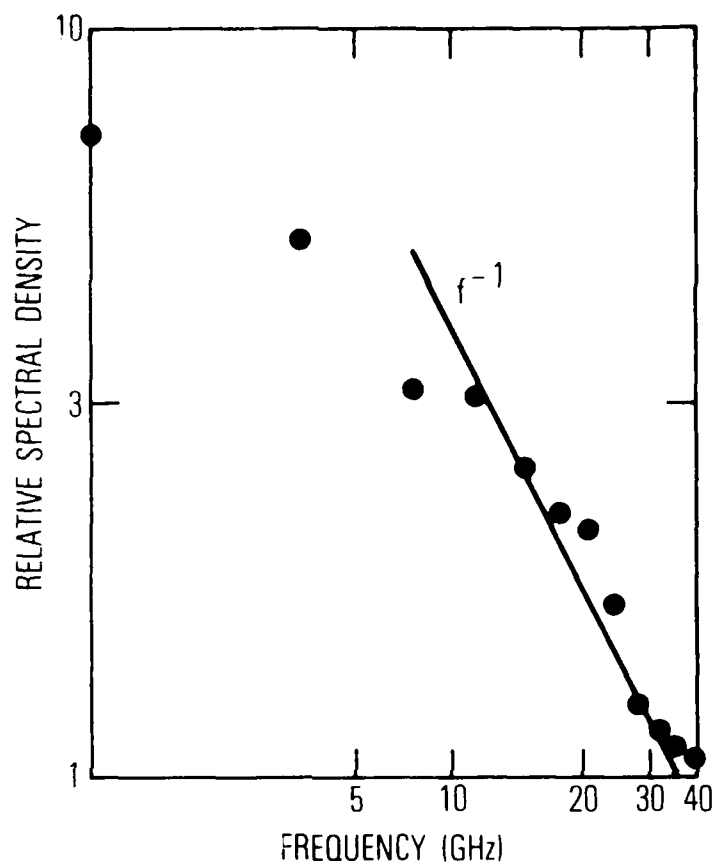
Figure 15.    Insertion Gain of 0.5-μm-Gate FET in Split Test Fixture.

Figure 16. Scattering Parameters of 0.5-μm-Gate FET in Planar Test Fixture.
(a) and (d) correspond to the pulse-response measurements of
Figures 9(a) and 10(d), respectively.  Open circles -
manufacturer's test data; solid circles - our data.

fixtures used. In particular, the source connection in our planar test fixture was to a pad with a width-to-substrate-thickness ratio of 3, which yields a 25-ohm impedance when the connection is considered as a transmission line. Variations in bond wire lengths probably could also have a considerable effect on the reflection measurements. In spite of these problems, the agreement between the two sets of scattering parameters is fairly good for the transmission measurements.

Figure 16(c) is a polar plot of $S_{21}$ that compares the picosecond opto-electronic data with the manufacturer's measurements. The fit over the 6 to 20-GHz region is quite good, with somewhat less gain indicated in our measurements. This may be due to the large source impedance in our test fixture. The phase factors agree very well, indicating that the two methods of measuring the propagation delay give the same result. Beyond the bandwidth limit of the manufacturer's specifications, the picosecond optoelectronic data cross through the 0-dB gain line at about 27 GHz, which is typical for a GaAs FET with a 0.5-μm gate. The complicated double resonance at 50 to 60 GHz is attributed to the quarter-wave resonances of the gate and drain bond wires. The data continue to be well above the noise level out beyond 60 GHz.

Figure 16(b) is a polar plot of $S_{12}$ calculated from the data of Figure 9(b). The fit to the manufacturer's measurements is fairly good at low frequencies, although considerably more phase shift occurs at frequencies approaching 20 GHz. At higher frequencies the same resonances seen in the $S_{21}$ data appear near 40 and 60 GHz.

Figures 16(a) and (d) show the Smith charts for $S_{11}$ and $S_{22}$, respectively. In both plots the data beyond about 35 GHz fall within a very small region on the chart, so the data were truncated there to avoid congestion. The poor fit between the picosecond optoelectronic data and the manufacturer's specifications is probably due to differences in the way the FET was bonded to the surrounding circuit. The main features of our results can be understood in terms of the time-domain data [Figures 9(a) and (d)], which in both cases consist of a reflection at the microstrip/wire-bond interface, followed about 25 psec later by a broad peak representing the reflection from the device itself. This transforms into low-amplitude frequency components at around 20 GHz, where points on a wave separated by 25 psec are of opposite polarity. The scattering-parameter amplitudes rise again beyond this point and

converge on a small region of the chart. This is because all the high-frequency components arise from the relatively sharp reflection from the interface rather than from the broad device reflection. The reference plane is at this interface, so that the temporal origin is at this sharp reflection peak. Thus there is no propagation delay, which means there is no phase shift as a function of frequency. This leads to the congested group of high-frequency points near the real axis. The Smith charts of $S_{11}$ and $S_{22}$ accurately reflect the main features of the interface between the device and the microstrip circuit of the test fixture.

The preliminary scattering parameters of the 0.3-μm-gate FET shown in Figure 17 correspond to the temporal response measurements shown in Figure 12. Since the switches were not adequately calibrated, the results for $S_{21}$ are shown as relative amplitudes. The characteristics of the reflection measurements are substantially different here from those for the 0.5-μm-gate FET. Since the reflection at the wire bond is more complex and better resolved than in the previous measurements, these differences are not surprising. The rapid changes in polarity indicate the existence of a resonance at 100 GHz, which is most likely due to the passage of the wide-bandwidth pulse through the RLC network at the wire-bond/FET interface. The polar plot of the gain of the device [Figure 17(c)] during transmission of a pulse from the gate to the drain shows a 3-dB point beyond 40 GHz, in accordance with the specifications of the device. The reflection measurements also show that the device is highly reflective at low frequencies. This, coupled with the problem of the Schottky barrier formed at the gate-channel interface, accounts for the lack of gain in the device. Regardless of these problems, however, these scattering parameters accurately reflect the main features of the temporal response of the FET.
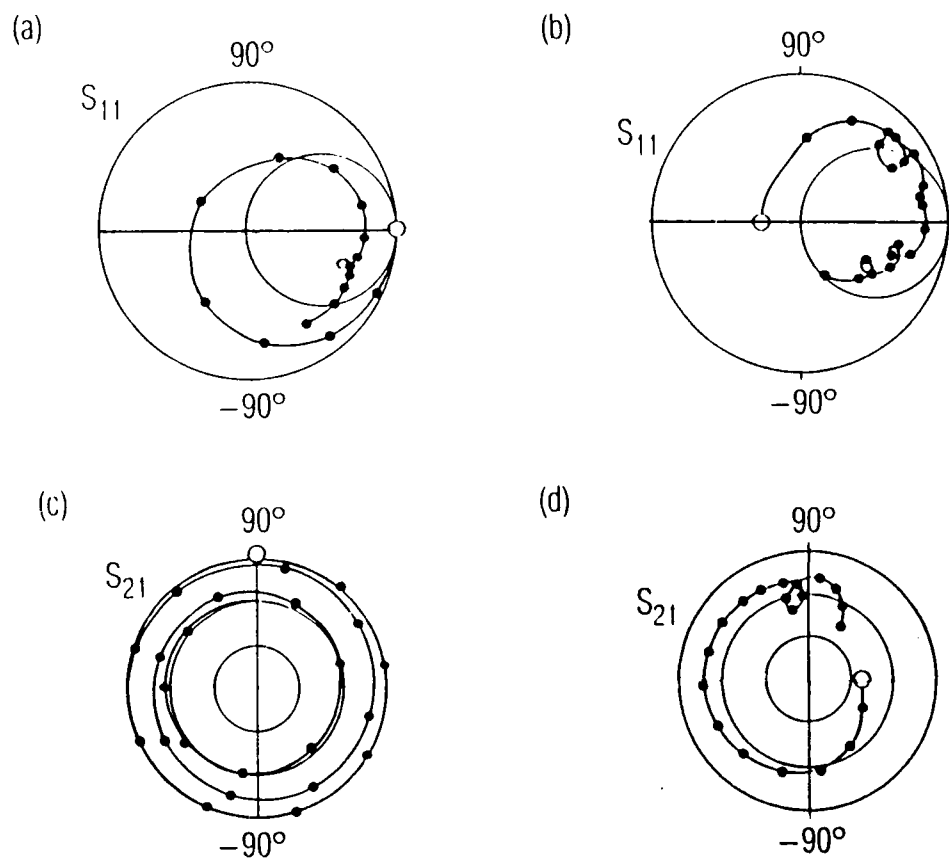
Figure 17. Scattering Parameters of 0.3-μm-Gate FET in Split Test Fixture.
(a) and (d) correspond to the pulse-response measurements of 12(a)
and 12(d), respectively.  Open circle - "dc" reponse; data points
separated by 2.9 GHz.  The solid line passing through the points is
to aid the eye.

44

# V. IMPROVEMENTS IN THE SYSTEM

The best improvement that can be made in this system is to shorten the picosecond electrical pulses and sampling apertures that are generated photoconductively. Shorter electrical pulses can be generated and sampled by shorter optical pulses, provided that the lifetime of the photogenerated carriers can also be shortened. Even if these pulses can be reduced indefinitely, however, we must still contend with temporal widths dominated here by the geometry of the switches. One can reduce these effects by reducing the size of the gap and by using thinner substrates to reduce the RC lifetimes associated with the geometry of the switch.[21]

By producing shorter pulses we can more clearly resolve features such as the optoelectronic autocorrelation from the reflection at the wire bonds. The shorter pulses will, however, become distorted more rapidly as they propagate along the waveguide.[19] Consequently, we must also reduce the length of the microstrip transmission line from the switches to the wire bond, which will reduce the increased effects of dispersion on the propagation of these shorter pulses.

Since the picosecond optoelectronic measurements are time-domain measurements transformed to the frequency-domain, any uncertainty in the temporal origin transforms to an uncertainty in the phase. Consequently, for an uncertainty in the temporal origin of $\Delta t$, the corresponding uncertainty in the phase is

$$\Delta\phi = 2\omega\Delta t = 4\pi\nu\Delta t \tag{1}$$

If we assume that the uncertainty in the temporal origin is ~0.1 of the autocorrelation width, then the uncertainty in the phase is

$$\Delta\phi \approx 0.4\pi\nu\tau \tag{2}$$

where $\tau$ is the temporal autocorrelation width. Equation (2) is plotted in Figure 18, which demonstrates the resulting phase error as a function of autocorrelation width. Since modern network analyzers obtain amplitude and phase information out to ~100 GHz with phase uncertainties of 10 to 20 degrees, we need autocorrelation widths of 1 to 2 psec to be competitive.
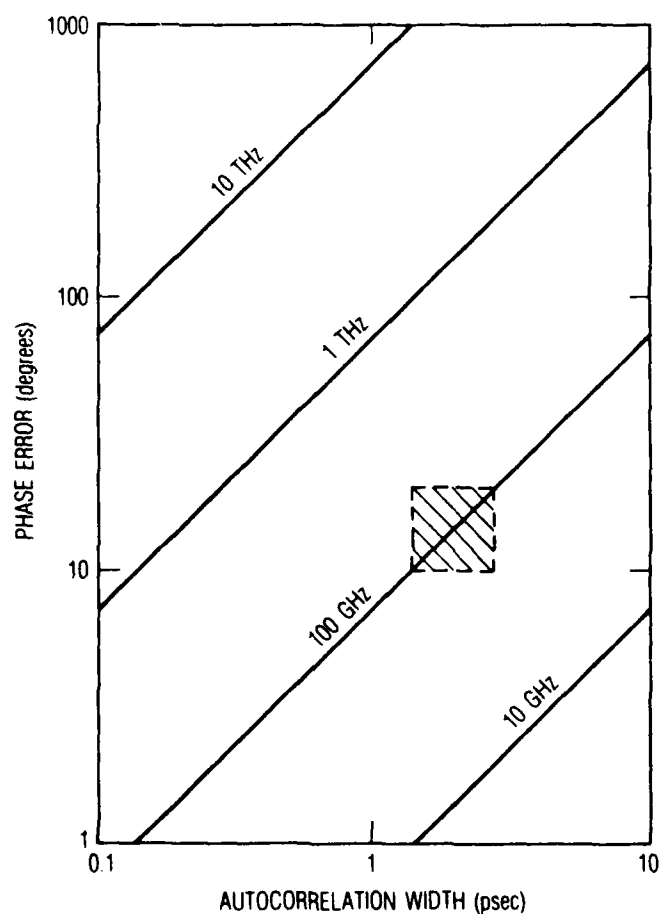
45

Figure 18. Phase Error Associated with the Picosecond Optoelectronic Measurement Technique as a Function of Optoelectronic Autocorrelation Width. This assumes that the temporal origin can be determined to within one-tenth of the autocorrelation width.

The generation of shorter electrical pulses and sampling apertures must also be accompanie by an improved temporal resolution in the translation stage of the excite-and-probe system. A stepping-motor translation-stage system coupled to an A/D converter of a microprocessor can provide femtosecond resolution with similar backlash and jitter.

We are in the process of adding a cavity dumper to our synchronously pumped dye-laser system. This will allow us to obtain higher peak powers out of the system, as well as to to vary the repetition rate. Varying the repetition rate will allow us to investigate the nature of long-lived transients within our system, as well as to determine the origin of the background seen in some of the measurements. Increasing the peak power will allow us to measure nonlinear effects in devices such as these FETs[22] and produce shorter optical pulses by using a fiber-grating pulse compressor.

We are presently incorporating improvements in the design of the test fixture holder that will allow better access to the microstrip transmission lines and lessen the effects of reflections at the bulkhead SMA connectors. The photoexcitation of the switch produces transients on the side transmission lines as well as on the control microstrips. These transients propagate through the system and are partially reflected at every interface, including the bulkhead connectors, which have a dc to 18-GHz bandwidth. By replacing these with the new OS-50 or OS-75 connectors, which have bandwidths in excess of 50 and 75 GHz, respectively, we can reduce the magnitude of the reflection at these interfaces, with the result being cleaner, more precise measurements.

We intend to use high-frequency modulation techniques to operate at a spectral region where the amplitude and phase noise of the system are minimized. Even at a few kilohertz the noise from the laser system should be substantially less than the 1 kHz at which we presently operate.

The test fixture is a very important component for device diagnostics, since it determines the circuit that surrounds the device. The split test fixture used in our studies is quite suitable for some devices, such as vertical FETs or permeable base transistors. In these devices the ground contact is on the bottom, conveniently situated for the split fixture. In the standard planar FETs, the source pads are on the top at either side, and low-impedance connection to the ground plane represents a problem in designing integrated circuits as well as test fixtures. One possible solution is the

47

use of a coplanar-waveguide transmission-line structure in which the ground plane is located on either side of the central conductor; we are investigating the use of such a coplanar waveguide structure for picosecond optoelectronic device diagnostics.[23]

# VI. COMPARISON

Microwave vector network analyzers that are commercially available can measure the complex scattering parameters of devices out to nearly 115 GHz. These systems can measure a device's response at any frequency that falls within one of the bands available from the network analyzer. Measurement at frequencies higher than 26.5 GHz requires external mixers for generation and detection, which increases the measurement system's cost and complexity. Complicated calibration procedures must be used to de-embed the device's response from the response of the entire test configuration, which includes the device, the test fixture, transmission lines, etc. These procedures rely on measurements using standards that must be changed as one changes from band to band of frequencies. Relative calibration between bands is thus very complex. Any thermal drift in the room will affect these measurements, and any thermal drift in the device can destroy even the most precise calibrations. Finally, network analyzers will yield only small-signal scattering parameters, and not the large-signal scattering parameters that may be more useful for devices such as power FETs.

Sampling oscilloscopes are widely used to sample ultrafast electronic transients, but are limited to risetimes of 25 psec or longer. When used as a time-domain reflectometer, a sampling scope will typically distort the waveform near the edge of an ultrafast step by as much as 20% peak-to-peak. Hamamatsu now offers a sampling optical oscilloscope with rise/fall times of less than 10 psec, a dynamic range of 30 dB, and a 4-MHz sampling rate.[24] The system requires a direct optical input, but it could be used in conjunction with ultrafast electro-optical sampling and continuous-wave probe beams to extract information about ultrafast electrical transients generated either photoconductively or electrically.

Picosecond optoelectronic techniques can measure subpicosecond rise and fall times that correspond to bandwidths in excess of 1 THz, but conversion of this data to the frequency domain yields a discrete spectrum with inter-frequency intervals equal to the inverse of the total temporal window of the measurement. For example, our translation stage is capable of 8.3 cm of travel, which corresponds to ~550 psec of time delay over which the transient response can be measured. Consequently, the frequency spectrum corresponding

to this time delay would have discrete components every 1.82 GHz. The first two components yielded by the FET are the dc component and the component at 1.82 GHz. One can obtain information at frequencies lower than 1.82 GHz only by measuring over longer time delays. This is not the only limitation, however. If a reflection from some element within the test fixture, the test fixture holder, or the transmission lines, or from connections outside the fixture holder, can propagate back into the system during the measurement window, it can obscure or deform some real signal. Consequently, the measurement window is the window over which spurious signals are introduced by elements other than the device under test, and can be identified and separated from the signal of interest.

# VII. MODELS

Early models of GaAs FETs were based on equivalent circuits that featured lumped elements consisting of resistors, capacitors, inductors, etc. These models have been widely used to model the response of GaAs FETs at relatively low frequencies (from dc to 26 GHz) and have displayed a great deal of utility.[25] When these lumped-element models are used to fit the response of high-frequency FETs, a suitable fit at high frequencies can be obtained only over a narrow bandwidth and the fit at lower frequencies is not very good. More sophisticated models, which include the transport of carriers within the device, the macroscopic circuit elements, and even the propagation of electro-magnetic waves along features of the device (e.g., along the width of the gate), have been developed.[26] These models show that in the real three-dimensional device, all of these effects must be included to model successfully the response of wide-bandwidth devices, even in the low-frequency regime. Consequently, measurement techniques that intrinsically yield reliable amplitude and phase information across wide bandwidths take on even more importance.

## VIII. CONCLUSIONS

We have illustrated the application of picosecond optoelectronics to high-frequency device diagnostics by characterizing a GaAs FET. Pulse-response measurements were transformed into scattering parameters that completely define the device's performance in the linear regime. A bandwidth of greater than 60 GHz (more than twice that of conventional CW diagnostic techniques) results from the application of pulse generation and sampling techniques based upon the use of ultrashort laser pulses. De-embedding is also simplified, because the pulses are generated and sampled within a few millimeters of the device being tested. These advantages make picosecond optoelectronics a very promising technique for device diagnostics in the millimeter wave region.

In addition to the capabilities we have illustrated in measuring the linear properties of devices, picosecond optoelectronics can be very useful in studying nonlinear devices such as power FETs. In nonlinear systems, frequency-domain analysis is not valid and direct time-domain analysis is necessary. The current theoretical models of nonlinear effects in solid-state devices are quite cumbersome, and contributions from time-domain experiments on nonlinear devices may lead to a better understanding of nonlinear effects.

# REFERENCES

1. L. Deardon, G. Miner, and M. Sayed, <u>1986 IEEE MTT-S Digest</u>, pp. 385-388.

2. Gould Electronics Data Sheet MPD0408 (August 1986).

3. H. Jaeckel et al., <u>IEEE Electron Device Letters EDL-7</u>, 522-524 (1986).

4. R. A. Murphy, in <u>Picosecond Electronics and Optoelectronics</u>, eds. G. A. Mourou, D. M. Bloom, and C.-H. Lee (Springer-Verlag, New York, 1985), pp. 38-45.

5. D. R. Dykaar et al. in <u>Ultrafast Phenomena V</u>, eds. G. R. Fleming and A. E. Siegman (Springer-Verlag, New York, 1986), pp. 103-106.

6. T. C. L. G. Sollner, E. R. Brown, and W. D. Goodhue, in <u>Picosecond Electronics and Optoelectronics</u>, eds. C.-H. Lee and F. J. Leonberger (Springer-Verlag, New York, 1987), in press.

7. G. A. Mourou, in <u>Picosecond Electronics and Optoelectronics</u>, eds. C.-H. Lee and F. J. Leonberger (Springer-Verlag, New York, 1987), in press.

8. Adapted from D. Handlon and L. Ulrich, <u>Microwave System News and Communications Technology</u> (September 1986), pp. 93-102.

9. Tektronix catalog (1986), pp. 230-237.

10. J. R. Andrews, in <u>Picosecond Electronics and Optoelectronics</u>, eds. C.-H. Lee and F. J. Leonberger (Springer-Verlag, New York, 1987), in press.

11. D. H. Auston, <u>Appl. Phys. Lett.</u> <u>26</u>, 101-103 (1975); D. H. Auston, A. M. Johnson, P. R. Smith, and J. C. Bean, <u>Appl. Phys. Lett.</u> <u>37</u>, 371-373 (1980); P. R. Smith, D. H. Auston, and W. M. Augustyniak, <u>Appl. Phys. Lett.</u> <u>39</u>, 739-741 (1981).

12. D. R. Grischkowsky et al., in <u>Picosecond Electronics and Optoelectronics</u>, eds. C.-H. Lee and F. J. Leonberger (Springer-Verlag, New York, 1987), in press.

13. K. E. Meyer and G. A. Mourou, in <u>Ultrafast Pheomena IV</u>, eds. D. H. Auston and K. B. Eisenthal (Springer-Verlag, New York, 1984), pp. 406-408.

14. F. E. Doany, D. Grischkowsky, and C.-C. Chi, in <u>Picosecond Electronics and Optoelectronics</u>, eds. C.-H. Lee and F. J. Leonberger (Springer-Verlag, New York, 1987), in press.

15. E. Walters, <u>Microwave Journal</u> <u>30</u>, 155-160 (1987).

16. D. E. Cooper and S. C. Moss, <u>IEEE J. Quantum Electron.</u> <u>QE-22</u>, 94-101 (1986).

17. A. M. Johnson and W. M. Simpson, <u>Opt. Lett.</u> <u>8</u>, 554-556 (1983).

18. J. R. Andrews, _Proc. IEEE_ 66, 414-423 (1978).

19. D. E. Cooper, _Appl. Phys. Lett._ 47, 33-35 (1985).

20. A. M. Nicolson et al., _IEEE Trans. Microwave Theory Tech._ 20, 3-9 (1972).

21. R. J. Manning and J. R. Hill, _Appl. Phys._ B-38, 17-21 (1985).

22. V. Bruckner and F. Kerstan, _Phys. Stat. Sol._ A-91, K179-K183 (1985).

23. C. P. Wen, _IEEE Trans. Microwave Theory Tech._, MTT-17, 1087-1090 (1969);
    J. K. A. Everard and J. E. Carroll, _Proc. IEEE_ 130, Pt. I, 5-16, (1983).

24. _Laser Focus/Electro-Optics_ (December 1986), p. 52.

25. H. Fukui, _Bell System Tech. J._ 58, 771-797 (1979).

26. W. Heinrich and H. L. Hartnagel, _IEEE Trans. Microwave Theory Tech._
    MTT-35, 1-8 (1987).

## LABORATORY OPERATIONS

The Aerospace Corporation functions as an "architect-engineer" for national security projects, specializing in advanced military space systems. Providing research support, the corporation's Laboratory Operations conducts experimental and theoretical investigations that focus on the application of scientific and technical advances to such systems. Vital to the success of these investigations is the technical staff's wide-ranging expertise and its ability to stay current with new developments. This expertise is enhanced by a research program aimed at dealing with the many problems associated with rapidly evolving space systems. Contributing their capabilities to the research effort are these individual laboratories:

Aerophysics Laboratory: Launch vehicle and reentry fluid mechanics, heat transfer and flight dynamics; chemical and electric propulsion, propellant chemistry, chemical dynamics, environmental chemistry, trace detection; spacecraft structural mechanics, contamination, thermal and structural control; high temperature thermomechanics, gas kinetics and radiation; cw and pulsed chemical and excimer laser development including chemical kinetics, spectroscopy, optical resonators, beam control, atmospheric propagation, laser effects and countermeasures.

Chemistry and Physics Laboratory: Atmospheric chemical reactions, atmospheric optics, light scattering, state-specific chemical reactions and radiative signatures of missile plumes, sensor out-of-field-of-view rejection, applied laser spectroscopy, laser chemistry, laser optoelectronics, solar cell physics, battery electrochemistry, space vacuum and radiation effects on materials, lubrication and surface phenomena, thermionic emission, photo-sensitive materials and detectors, atomic frequency standards, and environmental chemistry.

Computer Science Laboratory: Program verification, program translation, performance-sensitive system design, distributed architectures for spaceborne computers, fault-tolerant computer systems, artificial intelligence, micro-electronics applications, communication protocols, and computer security.

Electronics Research Laboratory: Microelectronics, solid-state device physics, compound semiconductors, radiation hardening; electro-optics, quantum electronics, solid-state lasers, optical propagation and communications; microwave semiconductor devices, microwave/millimeter wave measurements, diagnostics and radiometry, microwave/millimeter wave thermionic devices; atomic time and frequency standards; antennas, rf systems, electromagnetic propagation phenomena, space communication systems.

Materials Sciences Laboratory: Development of new materials: metals, alloys, ceramics, polymers and their composites, and new forms of carbon; non-destructive evaluation, component failure analysis and reliability; fracture mechanics and stress corrosion; analysis and evaluation of materials at cryogenic and elevated temperatures as well as in space and enemy-induced environments.

Space Sciences Laboratory: Magnetospheric, auroral and cosmic ray physics, wave-particle interactions, magnetospheric plasma waves; atmospheric and ionospheric physics, density and composition of the upper atmosphere, remote sensing using atmospheric radiation; solar physics, infrared astronomy, infrared signature analysis; effects of solar activity, magnetic storms and nuclear explosions on the earth's atmosphere, ionosphere and magnetosphere; effects of electromagnetic and particulate radiations on space systems; space instrumentation.